

Vertical separation of surface folding, earthquake faulting, and aftershocks in the Zagros Simply Folded Belt (Iran)

M. Roustaei¹, E. Nissen², M. Abbassi¹, M. Ghorashi³, A. Gholamzadeh¹,
M. Tatar¹, F. Yamini-Fard¹, E. Bergman⁴, J. Jackson² and B. Parsons⁵

¹ *International Institute of Earthquake Engineering and Seismology, PO Box 19395-3913, Tehran, Iran*

² *COMET, Bullard Laboratories, Madingley Road, Cambridge CB3 0EZ, UK*

³ *Geological Survey of Iran, PO Box 13185-1494, Tehran, Iran*

⁴ *Department of Physics, University of Colorado at Boulder, Boulder, CO 80309-0390, USA*

⁵ *COMET, Department of Earth Sciences, Parks Road, Oxford OX1 3PR, UK*

E-mail: ekn20@cam.ac.uk

Accepted 2008 February 1. Received 2008 January 1; in original form 2007 September 30

SUMMARY

The 25 March 2006 Fin earthquakes (M_w 5.7, 5.5, 5.2, 5.0, 4.9) provide an ideal opportunity to investigate buried reverse faulting in the Zagros fold-and-thrust belt, southwestern Iran. Modeling ground displacements measured with radar interferometry, we find that both N- and S-dipping model reverse faults can reproduce the observed fringe patterns. Despite the uncertainty in fault orientation, we can constrain the vertical extents of rupture to between ~ 5 and ~ 10 km, consistent with the 8 km centroid depth of the largest earthquake. This places the faulting within lower parts of the sedimentary cover, possibly between known detachment levels in the Gurpi marls and Hormuz salt, although lower parts of the fault may have ruptured into the uppermost basement. Using our models we are also able to constrain the pattern of

co-seismic surface uplift, which is centered not on any anticline but on the Fin syncline. This suggests that the whaleback anticlines which dominate the topography of the Zagros Simply Folded Belt are decoupled from the buried reverse faults which dominate its seismicity. Finally, we investigate the distribution of locally-recorded aftershocks in the weeks following the main earthquakes. Concentrated at depths of $\sim 10\text{--}20$ km, these lie within the crystalline basement rather than the sedimentary cover. The vertical separation between the main earthquakes and these smaller aftershocks indicates a non-uniform vertical distribution of strain within the seismogenic layer.

1 INTRODUCTION

The Zagros mountains trend for ~ 1500 km across SW Iran and are one of the major ranges of the Alpine-Himalayan belt (Fig. 1a). Formed by the closure of the Neo-Tethys ocean and the subsequent continental collision, starting in the Miocene (McQuarrie et al., 2003), between the Arabian Shield and central Iran, the Zagros range currently accommodates almost half of the N–S shortening between the Arabia and Eurasia, which is 25 mm yr^{-1} at 56° E (Vernant et al., 2004). The suture between former rocks of the Arabian continental margin and igneous and metamorphic rocks of central Iran lies in the High Zagros, but shortening is currently concentrated within the lower, Zagros Simply Folded Belt (ZSFB), which is one of the most seismically active fold-and-thrust belts in the world (Fig. 1a).

The ZSFB contains a thick sequence of Arabian passive margin sediments which spans the entire Phanerozoic (Fig. 1b), and which exerts a strong control on the style of deformation. Most earthquakes in the ZSFB have reverse-faulting mechanisms and centroid depths of less than ~ 20 km, but these rarely rupture the surface, probably because prominent salt layers within the sedimentary cover act as barriers to rupture (e.g. Jackson & Fitch, 1981; Berberian, 1995; Talebian & Jackson, 2004). Shortening at the surface is instead accommodated by folding, producing spectacular whaleback anticlines and synclines which dominate the topography of the region. These folds are often roughly concentric, have a typical width of ~ 10 km, and can be more than 100 km in length.

Because of the lack of surface faulting, most previous work on the active tectonics of the ZSFB comes from earthquake seismology. However, key questions remain unresolved, partly because of poor constraints on the thickness of the sedimentary cover, which is ~ 11 km in the central ZSFB (Hatzfeld et al., 2003) but may vary considerably locally, and partly because of uncertainties in earthquake epicentres and depths, which are in the order of 10–15 km and ~ 4 km (for waveform-modeled events), respectively (Engdahl et al., 2006).

In this paper, we focus on two particular issues that are not yet resolved. The first concerns the vertical distribution of seismogenic faulting within the upper crust: do the blind, reverse-faulting earthquakes rupture the sedimentary cover or the underlying, crystalline basement (or both)? The second concerns the relationship between these reverse faults and the surface geology. In several other regions of intracontinental shortening, anticlines form above concealed reverse faults as a consequence of diminished slip within the uppermost sedimentary layers (e.g. Yielding et al., 1981; Stein & King, 1984; Walker et al., 2003). Do the whaleback anticlines of the Zagros SFB also grow above buried reverse faults, or are folding and faulting completely decoupled?

We address these problems using Synthetic Aperture Radar interferometry (InSAR), a satellite-based technique which maps line-of-sight ground displacements by differencing before- and after-radar images of the Earth's surface (e.g. Bürgmann et al., 2000). These maps, or interferograms, cover wide areas with tens-of-meters resolution and sub-centimeter precision. Coseismic ground displacements measured in this way can be compared with the surface geology to reveal any spatial connection between the earthquake deformation and folding. Because the wavelength of a coseismic surface signal depends on the depth at which slip occurs, these line-of-sight displacements can also be modeled using elastic dislocation theory (Okada, 1985) to determine the earthquake source parameters, including the top and bottom depths of the ruptured fault plane (e.g. Feigl et al., 1995).

Since InSAR was developed during the early 1990's there have been unusually few earthquakes in the ZSFB compared to previous decades; there is also a relative scarcity of SAR data available for the region (Lohman & Simons, 2005). As a result, few earthquakes in the ZSFB have been studied with InSAR. Lohman & Simons (2005) locate four earthquakes in the region,

but these are relatively small events (M_w 4.7–5.4) and in each case displacements are measured in a single viewing geometry, preventing a full assessment of the source parameters. Nissen et al. (2007) studied the larger (M_w 6.0), 2005 Qeshm Island earthquake using data from both ascending (moving north) and descending (moving south) satellite orbit tracks, providing an additional component of the displacement vector. Elastic dislocation models of this earthquake placed fault slip at depths of ~ 4 km to ~ 8 km, probably mostly within the sedimentary cover. Although coseismic uplift was centered on an anticline, the complicated surface structure of Qeshm Island (consisting of orthogonal sets of fold axes) obscured the connection between faulting at depth and folding at the surface.

2 THE 25 MARCH 2006 FIN EARTHQUAKES

On 25 March 2006 at 07:29 UTC (10:59 local time), a M_w 5.7 earthquake struck the Fin region in the south-eastern ZSFB (Figs. 1c & 2a). This earthquake was followed by aftershocks at 09:55 (M_w 5.5), 10:00 (M_w 5.2), 11:02 (M_w 5.0) and 12:13 UTC (M_w 4.9). There were no reports of injuries or loss of life, but there was minor damage to buildings in the village of Bonab. The earthquakes also triggered landsliding in the area between Bonab and Fin, but there were no indications of any surface ruptures.

Focal mechanisms for all five earthquakes are available from the Global CMT catalog (Dziewon-ski et al., 1981). These indicate almost pure reverse slip on E–W striking fault planes, which dip either $\sim 30^\circ$ N or $\sim 60^\circ$ S. By modeling teleseismically-recorded P and SH bodywaves (Molnar & Lyon-Caen, 1989), we obtain improved source parameters and centroid depths for the largest two events (Table 1 and Figs 4 & 5, supplementary material). Our models have similar strikes, dips and rakes to the Global CMT mechanisms, and have centroid depths of 8 ± 3 km and 4 ± 2 km. We also calculate improved relative locations for the largest two events using the hypocentroidal decomposition (HDC) method of Jordan & Sverdrup (1981). Our results place the 09:55 aftershock ~ 10 km ENE of the mainshock, consistent with rupturing of along-strike sections of the same fault zone.

The surface structure of the Fin region consists of a series of parallel, E–W trending folds

(Fig. 2b), and is relatively simple compared, for instance, with Qeshm Island. The 2006 Fin earthquakes therefore provide an ideal opportunity to study the connection between faulting and folding in the ZSFB. In Section 3, we measure coseismic surface displacements with InSAR and model them with elastic dislocation theory. Finally, in section 4, we use locally recorded seismic data to investigate the distribution of smaller aftershocks.

3 SYNTHETIC APERTURE RADAR INTERFEROMETRY (INSAR)

We constructed four interferograms spanning the 25 March 2006 earthquakes, using measurements from ESA's Envisat satellite (Table 2 and Fig. 6a–d, supplementary material). Three of these interferograms are constructed from descending satellite passes, with an \sim ENE-facing pointing vector (between the satellite and the ground) and a center-scene incidence angle of 23° (measured from the vertical). A fourth interferogram, produced from ascending satellite passes with a \sim WNW-facing pointing vector and a center-scene incidence angle of 41° , provides an additional component of the displacement vector. Full details of the data and processing are provided in the supplementary material.

All four interferograms display a clear, coseismic signal centered on the Fin syncline, \sim 20 km WSW of the town of Fin (Fig. 6a–d, supplementary material). In each case, the signal consists of an elliptical, WSW–ENE-trending pattern of displacements. These patterns contain two full fringes, indicating peak displacements of two radar wavelengths (or \sim 6 cm) toward the satellites. Although the peak displacements in the ascending-track interferogram are situated \sim 3–6 km west of those in the descending ones, the broad overlap of ascending and descending fringe patterns implies that line-of-sight displacements are dominated by vertical uplift, rather than any strike-slip component (e.g. Nissen et al., 2007). Some of the interferograms also display apparent displacements away from the satellite in areas just N and S of the ellipse patterns. However, because these are relatively small (only about half a fringe) compared to the amplitude of the atmospheric noise, we cannot be certain that these represent coseismic displacements.

There is no sharp boundary between displacements toward the satellites from the apparent displacements away from it, indicating that whatever slip occurred at depth did not reach the

surface. In cases of buried earthquakes, the surface projection of the fault is indicated by the most closely-packed fringes. For the Fin earthquakes, this would place the surface projection of faulting along either the northern or southern edge of the elliptical fringe pattern, although it is not immediately clear which.

After resampling the interferograms, we model the displacements using the method of Wright et al. (2003). Faulting is represented as a single, rectangular dislocation in an elastic half-space (Okada, 1985), with Lamé parameters ($\mu = \lambda = 2.8 \times 10^{10}$ Pa) that are consistent with the velocity structure calculated in the next section. At first, we assume uniform slip on this fault plane, and solve for the strike, dip, rake, amount of slip, latitude, longitude, length, and top and bottom depths of the fault, as well as a static shift in the measured displacements (to account for ambiguities in the zero-displacement level) and displacement gradients in the N–S and E–W directions (to account for residual orbital phase ramps). Our minimum-misfit parameters are given in Table 1 (Model A) and model interferograms are shown in Fig. 6e–f (supplementary material). The down-dip width of the model fault (~ 8 km) is small compared with its length (~ 21 km). Using the relationship $M_o = \mu Au$ and assuming $\frac{u}{L} \simeq 5 \times 10^{-5}$ (Scholz, 1982), the fault-plane dimensions of the largest, 07:29 and 09:55 earthquakes are probably ~ 7 km and ~ 5 km, respectively; we also know that these two events occurred along strike from one another (Section 2). Our InSAR-derived model is therefore likely to represent the combined displacements of these two earthquakes.

To investigate errors and trade-offs in our fault plane parameters, we model 100 synthetic datasets, created by perturbing the original data with noise characteristic of the undeformed parts of the interferograms (Wright et al., 2003). Some of the resulting fault-plane parameters include unrealistically high values of slip on very narrow fault planes, and we discount those results with more than 1 m slip. Around two thirds of the realistic inversion results have N-dipping fault planes; these are used to calculate the 1σ errors for model A in Table 1. Most of the rest of the realistic inversion results contain S-dipping fault planes, providing an alternative, S-dipping model outlined in Table 1 (Model B) and shown in Fig. 6e–f.

There are significant, $\sim 20^\circ$ discrepancies between the strike and rake of the InSAR-derived model faults and those of the bodywave solutions. To investigate this, we model the interferometric

data again, this time solving for slip on two separate faults whose strikes, dips and rakes are fixed to the values of the bodywave models. We also fix the slip on the two fault planes to 0.35 m and 0.25 m, values which are consistent with the bodywave moments (using $M_o = \mu Au$ and assuming $\frac{u}{L} \simeq 5 \times 10^{-5}$). The minimum-misfit parameters of these models are given in Table 1 (for model C we use the N-dipping bodywave nodal planes, and for model D we use the S-dipping nodal planes). We find that these models can successfully reproduce the observed, WSW–ENE elliptical fringe patterns, by offsetting the two faults in an en echelon fashion (Fig. 6g–j); the sense of offset is consistent with the relative locations yielded by the HDC method in Section 2. The discrepancies in strike and rake observed for the single-fault models may, therefore, reflect segmented, en-echelon faulting.

It is clear, from the arguments above, that we are unable to precisely constrain the orientation of the faulting from the surface displacements alone. However, what we are most interested in is the extents of slip at depth, and the relationship between the vertical uplift and the surface geology.

There are significant errors (more than 1 km at the 1σ level) in the top and bottom depths of both model A and B, reflecting a negative trade-off between slip and down-dip fault width. The errors for model C and D are around 0.5 km for the top depth and 1–2 km for the bottom depth; the amount of slip is fixed in these inversions (as well as the orientation of the faults), and these errors instead reflect other trade-offs, including one between the top and bottom depths of the fault plane and the latitude of its projected surface trace (a negative trade-off in the case of the N-dipping model C, but a positive one for S-dipping model D). Considering all four models together, the top depth is 5 ± 1.5 km, the bottom depth 9.5 ± 2 km, and the center of the faulting 7 ± 1 km. These figures are consistent with the 8 ± 3 km and 4 ± 2 km centroid depths obtained for the 07:29 and 09:55 earthquakes.

To further test how tightly constrained these depths are, we increase the size of each model fault, divide these fault planes into 2×2 km patches, and solve for distributed slip (Wright et al., 2003). In each case, we find that the vertical extents of slip are not significantly changed from the uniform slip models, with negligible slip above ~ 5 km and below ~ 10 km. This would suggest that faulting primarily ruptured the lower part of the sedimentary cover – possibly within a series

of relatively competent layers (the ‘Competent Group’) situated between the Hormuz salt and Gurpi marls, both well-known detachment horizons (Fig. 1b). However, given the trade-offs in fault parameters and the considerable uncertainties in the thickness of the sedimentary cover, it is not clear whether the earthquakes also ruptured into adjacent layers – either above, into the Cenozoic part of the sedimentary cover, or below, into the uppermost crystalline basement.

We can also use our elastic dislocation models to infer the pattern of vertical motions caused by the earthquakes. Fig. 2c shows the vertical displacements calculated for model A (equivalent maps for models B, C and D look very similar – after all, each model must account for the overlap of ascending- and descending-track fringe patterns – and so are not shown here). Surface uplift is centered on the southern limb of the Fin syncline, forming a pattern which is slightly oblique to the E-W trend of the fold axis. The Fin earthquakes therefore imply a decoupling between the buried reverse faults which dominate the seismicity of the ZSFB, and the surficial folding which governs the relief. The spectacular whaleback anticlines are likely to express the ~ 10 km half-wavelength folding of the thick, competent Asmari limestone, rather than any underlying reverse faults.

Interestingly, the peak uplift (>6 cm) coincides with a distinct ridge in the N-dipping, Neogene sediments that make up the southern limb of the Fin syncline. This may represent the surface expression of the reverse faulting that ruptured in the Fin earthquakes (even though this faulting does not control the large-scale folding of the upper sedimentary cover). However, without further investigation we cannot rule out other explanations, such as local, resistant bedding.

4 LOCAL RECORDING OF AFTERSHOCKS

In addition to our teleseismic and radar measurements of the Fin earthquake sequence, we also investigate the distribution of smaller aftershocks using data collected from a local network of portable, three-component seismometers. The five stations plotted on Fig. 2a were deployed on 12 April 2006 and recorded until 29 May 2006. These were complemented by a network of eighteen seismometers already deployed (since early March) in the area east of Fin, where an earlier, M_w 6.0 earthquake occurred on 28 February 2006. We use the same instruments and data processing techniques as Tatar et al. (2005).

In total, 192 aftershocks were recorded in the region shown Fig. 2a. 49 of these aftershocks have an azimuthal gap of $\leq 185^\circ$ and an RMS residual of ≤ 0.5 s, and we consider these events the most reliable. To locate their hypocenters, we followed the methodology of Tatar et al. (2005), first using a standard half-space model, then inverting the arrival times of the 49 best-recorded events to compute a best-fit, 1-D velocity structure. Finally, we calculate an improved, 2-D velocity model (Table 4, supplementary material) by inverting arrival times for a layered velocities, using randomly perturbed starting models to ensure convergence to the final structure. Because of the small number of readings and the poor azimuthal coverage of the temporary network, this model is unlikely to provide an accurate measure of the thickness of the sedimentary cover, but it does offer a useful gauge of the velocities and elastic properties of the upper crust, which we use for our bodywave and elastic dislocation models in the earlier sections.

The 49 best-recorded aftershocks are listed in Table 3 (supplementary material) and their depths shown in Fig. 3a. Vertical errors in these depths are always >3 km and often much higher (Fig. 3b), while horizontal errors in the aftershock locations are typically 3–10 km. Nevertheless, almost all of the hypocenters are situated at depths of 10–20 km, with more than half (and most of the best-located ones) between 15 and 20 km. Even accounting for the large errors, these aftershocks appear to be significantly deeper than the main earthquake rupture (~ 5 –10 km) and are probably concentrated within the crystalline basement. The clear, vertical separation between the main rupture and aftershocks indicates a non-uniform, short-term, vertical distribution of strain within the seismogenic layer. This may reflect the influence of the major detachment in the Hormuz salt, although similar vertical separations have been noted in a few other areas – inside and outside Iran – where detachment horizons are not thought to play such an important role (e.g. Tatar et al., 2005; Jackson et al., 2006; Semmane et al., 2005).

To investigate the relationship between the main faulting and the aftershocks further, we plot cross-sections through the aftershock hypocenters and our model faults (Fig. 3c & d). There are no clear indications that the aftershocks form a downward extension of the main faulting, though this may reflect the large uncertainties in hypocenter locations.

5 CONCLUSIONS

Coseismic surface displacements of the 2006 Fin earthquakes imply a decoupling of buried reverse faulting and surface folding in the Zagros Simply Folded Belt. There is also a vertical separation between the main earthquakes, which ruptured lower parts of the ~10 km-thick sedimentary cover, and locally-recorded aftershocks, which were concentrated within the underlying, crystalline basement.

References

- Berberian, M., 1995. Master blind thrust faults hidden under the Zagros folds: active basement tectonics and surface morphotectonics, *Tectonophys.*, **241**, 193–224.
- Bürgmann, R., Rosen, P. A., & Fielding, E. J., 2000. Synthetic Aperture Radar interferometry to measure the Earth's surface topography and its deformation, *Ann. Rev. Earth. Planet. Sci.*, **28**, 169–209.
- Dziewonski, A. M., Chou, T.-A., & Woodhouse, J. H., 1981. Determination of earthquake source parameters from waveform data for studies of global and regional seismicity, *J. Geophys. Res.*, **86**, 2825–2852.
- Engdahl, E. R., van der Hilst, R. D., & Buland, R., 1998. Global teleseismic earthquake relocation from improved travel times and procedures for depth determination, *Bull. Seismol. Soc. Am.*, **88**, 722–743.
- Engdahl, R. E., Jackson, J. A., Myers, S. C., Bergman, E. A., & Priestley, K., 2006. Relocation and assessment of seismicity in the Iran region, *Geophys. J. Int.*, **167**, 761–778.
- Feigl, K. L., Sargent, A., & Jacq, D., 1995. Estimation of an earthquake focal mechanism from a satellite radar interferogram: Application to the December 4, 1992 Landers aftershock, *Geophys. Res. Lett.*, **22**, 1037–1040.
- Hatzfeld, D., Tatar, M., Priestley, K., & Ghafory-Ashtiany, M., 2003. Seismological constraints on the crustal structure beneath the Zagros Mountain belt (Iran), *Geophys. J. Int.*, **155**, 403–410.
- Jackson, J. & Fitch, T., 1981. Basement faulting and the focal depths of the larger earthquakes in the Zagros mountains (Iran), *Geophys. J. Int.*, **64**, 561–586.

- Jackson, J., Bouchon, M., Fielding, E., Funning, G., Ghorashi, M., Hatzfeld, D., Nazari, H., Parsons, B., Priestley, K., Talebian, M., Tatar, M., Walker, R., & Wright, T., 2006. Seismotectonic, rupture process, and earthquake-hazard aspects of the 2003 December 26 Bam, Iran, earthquake, *Geophys. J. Int.*, **166**, 1270–1292.
- Jordan, T. H. & Sverdrup, K. A., 1981. Teleseismic location techniques and their application to earthquake clusters in the South-Central Pacific, *Bull. Seismol. Soc. Am.*, **71**, 1105–1130.
- Lohman, R. B. & Simons, M., 2005. Locations of selected small earthquakes in the Zagros mountains, *Geochem. Geophys. Geosyst.*, **6**, Q03001.
- McQuarrie, N., Stock, J. M., Verdel, C., & Wernicke, B. P., 2003. Cenozoic evolution of Neotethys and implications for the causes of plate motions, *Geophys. Res. Lett.*, **30**(20), 2036.
- Molinaro, M., Leturmy, P., Guezou, J.-C., Frizon de Lamotte, D., & Eshraghi, S. A., 2005. The structure and kinematics of the southeastern Zagros fold-thrust belt, Iran: From thin-skinned to thick-skinned tectonics, *Tectonics*, **24**, TC3007.
- Molnar, P. & Lyon-Caen, H., 1989. Fault plane solutions of earthquakes and active tectonics of the Tibetan Plateau and its margins, *Geophys. J. Int.*, **99**, 123–154.
- Nissen, E., Ghorashi, M., Jackson, J., Parsons, P., & Talebian, M., 2007. The 2005 Qeshm Island earthquake (Iran) – a link between buried reverse faulting and surface folding in the Zagros Simply Folded Belt?, *Geophys. J. Int.*, **171**, 326–338.
- Okada, Y., 1985. Surface deformation due to shear and tensile faults in a half-space, *Bull. Seismol. Soc. Am.*, **75**, 1135–1154.
- Scholz, C. H., 1982. Scaling laws for large earthquakes: consequences for physical models, *Bull. Seismol. Soc. Am.*, **72**, 1–14.
- Semmane, F., Cotton, F., & Campillo, M., 2005. The 2000 Tottori earthquake: A shallow earthquake with no surface rupture and slip properties controlled by depth, *J. Geophys. Res.*, **110**(B9), 03306.
- Stein, R. S. & King, G. C. P., 1984. Seismic Potential Revealed by Surface Folding: 1983 Coalinga, California, Earthquake, *Science*, **224**, 869–872.
- Talebian, M. & Jackson, J., 2004. A reappraisal of earthquake focal mechanisms and active short-

ening in the Zagros mountains of Iran, *Geophys. J. Int.*, **156**, 506–526.

Tatar, M., Hatzfeld, D., Moradi, A. S., & Paul, A., 2005. The 2003 December 26 Bam earthquake (Iran), Mw 6.6, aftershock sequence, *Geophys. J. Int.*, **163**, 90–105.

Vernant, P., Nilforoushan, F., Hatzfeld, D., Abbassi, M. R., Vigny, C., Masson, F., Nankali, H., Martinod, J., Ashtiani, A., Bayer, R., Tavakoli, F., & Chéry, J., 2004. Present-day crustal deformation and plate kinematics in the Middle East constrained by GPS measurements in Iran and northern Oman, *Geophys. J. Int.*, **157**, 381–398.

Walker, R., Jackson, J., & Baker, C., 2003. Surface expression of thrust faulting in eastern Iran: source parameters and surface deformation of the 1978 Tabas and 1968 Ferdows earthquake sequences, *Geophys. J. Int.*, **152**, 749–765.

Wright, T. J., Lu, Z., & Wicks, C., 2003. Source model for the M_w 6.7, 23 October 2002, Nenana Mountain Earthquake (Alaska) from InSAR, *Geophys. Res. Lett.*, **30**(18), 1974.

Yielding, G., Jackson, J. A., King, G. C. P., Sinvhal, H., Vita-Finzi, C., & Wood, R. M., 1981. Relations between surface deformation, fault geometry, seismicity, and rupture characteristics during the El Asnam (Algeria) earthquake of 10 October 1980, *Earth Planet. Sci. Lett.*, **56**, 287–304.

Data	Model	Strike	Dip	Rake	Slip (m)	Eastings (km)	Northings (km)	Length (km)	Top (km)	Bottom (km)	Centroid (km)	Moment (Nm)	M_w
Bodywaves	07:29 ¹	271°	30°	88°	-	-	-	-	-	-	8±3	4.7±2.0 ×10 ¹⁷	5.7
Bodywaves	09:55 ²	279°	45°	84°	-	-	-	-	-	-	4±2	1.9±0.5 ×10 ¹⁷	5.5
InSAR	A (1 fault)	248°±5	31°±11	65°±10	0.27±0.14	374.8±1.9	3040.9±2.3	21.5±2.4	4.6±1.3	8.4±1.3	6.5±1.2	11.2±1.7 ×10 ¹⁷	6.0
InSAR	B (1 fault)	73°±5	37°±5	102°±13	0.33±0.16	368.5±1.5	3058.3±1.8	19.0±2.7	5.6±1.2	10.5±1.2	8.0±0.7	12.1±2.0 ×10 ¹⁷	6.0
InSAR	C (2 faults) ³	271°	30°	88°	0.35	366.6±2.2	3036.4±1.9	14.1±2.3	6.1±0.6	8.7±1.1	7.4±0.8	7.1±1.5 ×10 ¹⁷	5.8
InSAR		279°	45°	84°	0.25	373.4±3.0	3044.9±2.1	9.9±2.3	4.4±0.7	10.5±2.2	7.4±1.2	5.6±1.4 ×10 ¹⁷	5.8
InSAR	D (2 faults) ³	93°	60°	91°	0.35	367.2±1.9	3053.2±0.8	14.0±2.5	5.2±0.5	9.8±1.6	7.5±1.0	7.0±1.4 ×10 ¹⁷	5.8
InSAR		107°	45°	95°	0.25	376.9±2.3	3058.1±1.5	11.4±1.7	4.8±0.5	9.3±1.4	7.1±0.9	5.1±1.3 ×10 ¹⁷	5.7

Table 1. Fault plane parameters for the 25 March 2006 07:29 and 09:55 UTC earthquakes, from modeling P and SH bodywaves and line-of-sight displacements. *Eastings* and *Northings* refer to the surface projection of the center of the model fault plane (in UTM zone 40 coordinates). *Top* and *Bottom* refer to the top and bottom depths of the model fault plane; *Centroid* refers to the centroid depth for the bodywave models, and the depth of the center of the fault plane for the InSAR-derived models. Errors in the bodywave depths and moments were estimated using the procedure of (Molnar & Lyon-Caen, 1989), while InSAR models are shown with 1σ errors calculated by inverting 100 datasets perturbed by realistic noise.

¹ the other nodal plane has strike 93°, dip 60° and rake 91°.

² the other nodal plane has strike 107°, dip 45° and rake 95°.

³ strike, dip and rake and slip fixed in inversion.

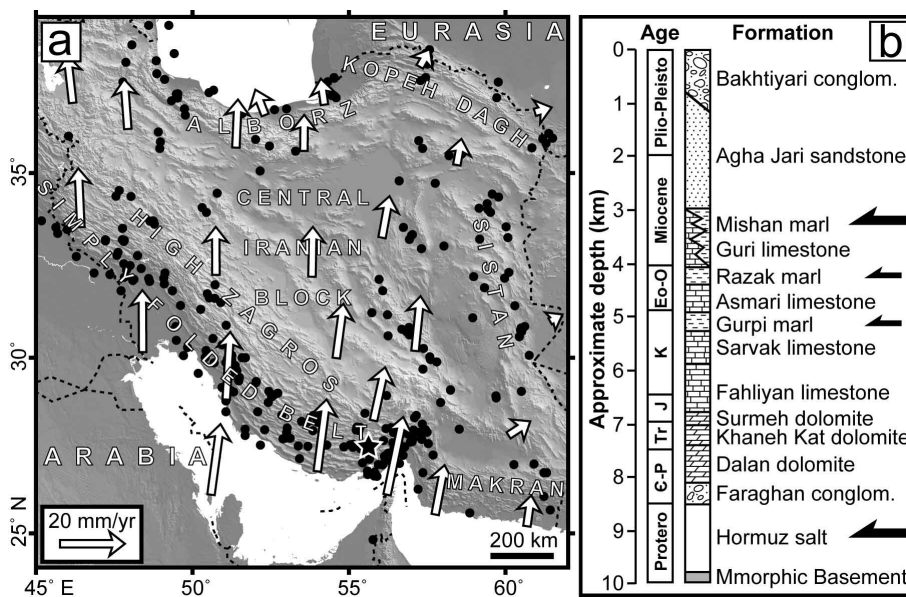


Figure 1. (a) Tectonic setting of the Zagros Simply Folded Belt. The black star represents the 25 March 2006 Fin earthquakes; black dots are other earthquakes listed in the Global CMT catalogue (1976–2008); and white arrows are GPS velocities relative to stable Eurasia from Vernant et al. (2004). (b) Simplified stratigraphic column for our study area in the SE Zagros, from Molinaro et al. (2005). The depths are poorly constrained and should be considered approximate, only. Possible décollement levels are picked out by black arrows.

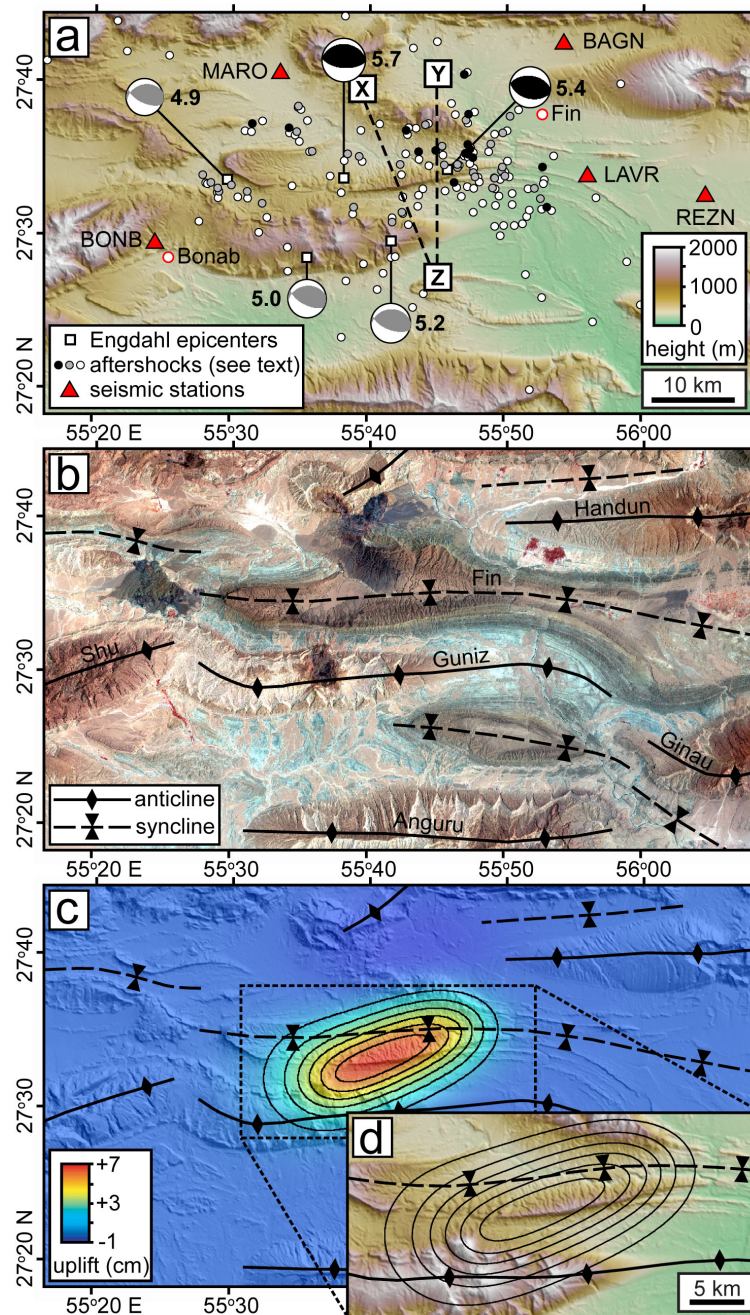


Figure 2. (a) Focal mechanisms of the 25 March 2006 earthquakes, locally-recorded aftershocks, and sunshaded Shuttle Radar Topography Mission (SRTM) digital topography. Black mechanisms are bodywave models of the largest two earthquakes and grey mechanisms are from the Global CMT catalog; the moment magnitude of each earthquake is plotted next to the focal sphere, and epicentres are from an updated version of the Engdahl et al. (1998) catalog. Black and grey dots are the best 49 locally-recorded aftershocks, black ones being those with vertical errors of ≤ 6 km (see Fig. 3); white dots are other locally-recorded events. (b) Landsat image (RGB 421) of the epicentral area, with major fold axes marked on in black lines. Vegetation appears red in this image. (c) Surface uplift predicted by our N-dipping, single-fault interferometric model (A), with contours at 1 cm intervals. (d) The same surface uplift contours plotted on topography.

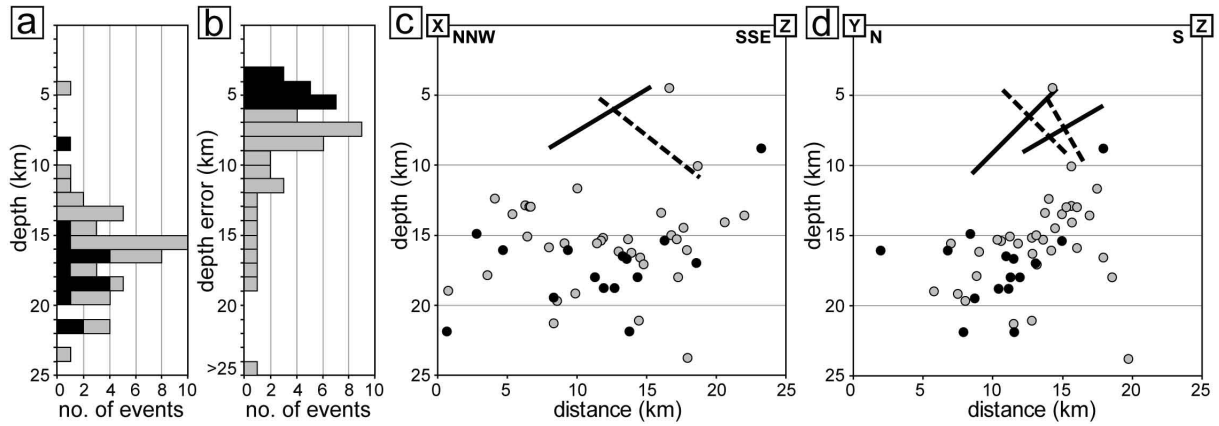


Figure 3. (a) Histogram showing hypocenter depths of the 49 best-recorded aftershocks; black bars represent those events with vertical errors of ≤ 6 km. (b) Vertical errors for the same, 49 aftershock hypocenters. Horizontal errors are mostly 3–10 km. (c) & (d) Cross-sections through the Fin region, showing projections of our model fault planes and the 49 best-recorded aftershock hypocentres onto the lines X–Y and X–Z (see Fig. 1). (c) is a section perpendicular to the strike of faults in model A (solid line) and B (dashed line). (d) is a N–S section, approximately perpendicular to the strike of faults in model C (solid lines) and D (dashed lines). Black circles are aftershocks with vertical errors ≤ 6 km, and grey circles are those with vertical errors > 6 km.

6 SUPPLEMENTARY MATERIAL

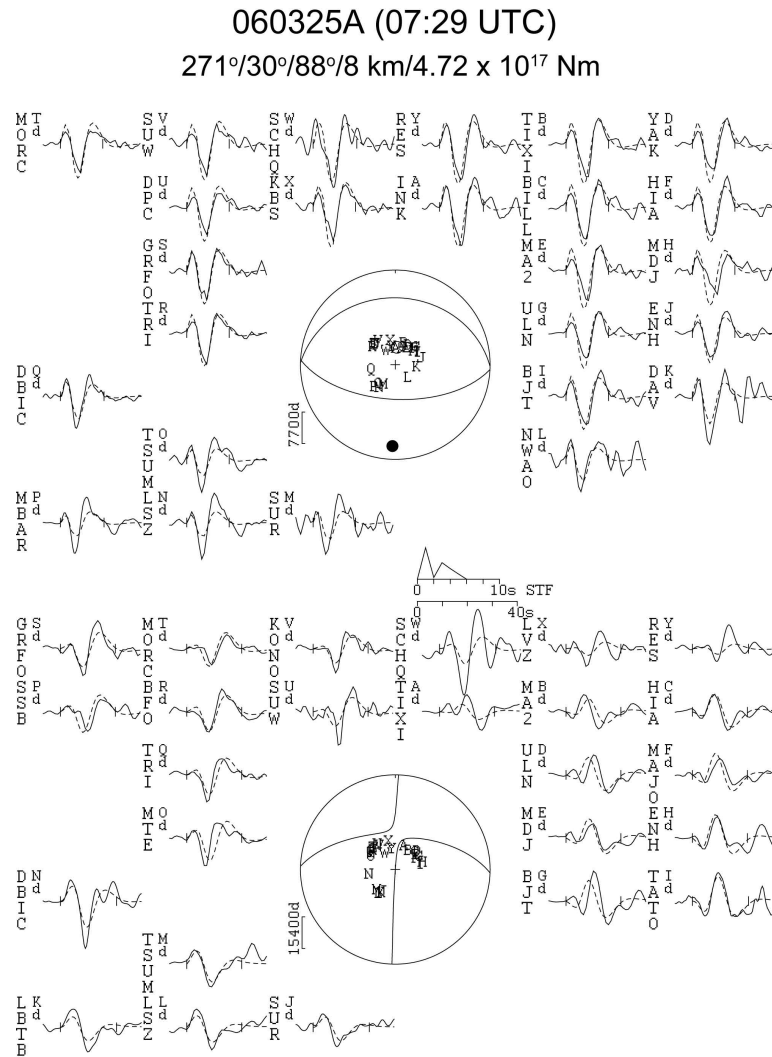


Figure 4. Minimum misfit solution for the first 25 March 2006 earthquake (07:29:01 UTC), calculated by inverting P and SH bodywaves for a point source in a half space of $V_p = 5.7 \text{ ms}^{-1}$, $V_s = 3.3 \text{ ms}^{-1}$ and $\rho = 2.6 \times 10^3 \text{ kg/m}^3$ (consistent with the elastic parameters used in the InSAR modeling). The focal spheres show P (top) and SH (bottom) nodal planes in lower hemisphere projections; closed and open circles represent the P-axes and T-axes respectively. Numbers beneath the header line are strike, dip, rake, centroid depth (km) and moment (Nm) of the earthquake. Observed (solid) and synthetic (dashed) waveforms are plotted around the focal spheres; the inversion window is indicated by vertical ticks, station codes are written vertically and station positions denoted by capital letters. The STF is the source time function, and the scalebar below it (in seconds) is that of the waveforms.

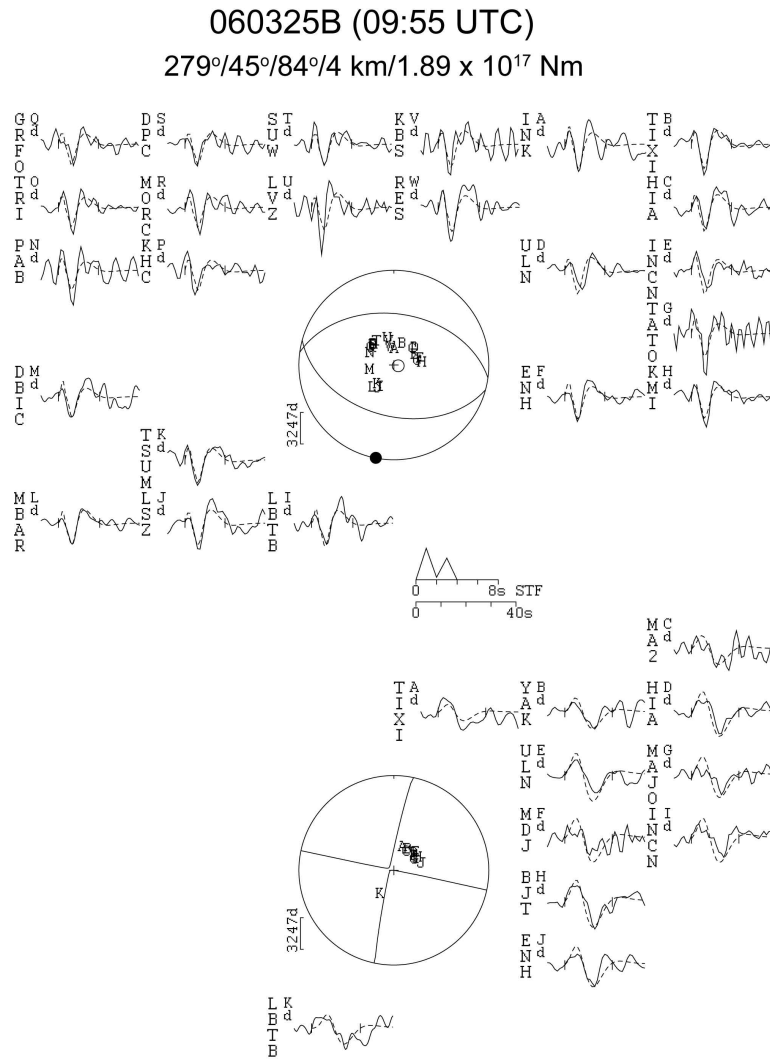


Figure 5. Minimum misfit solution for the second 25 March 2006 earthquake (09:55:16 UTC) from P and SH bodywave modeling. The layout is the same as for Fig. 4.

<i>Pass</i>	<i>Mode</i>	<i>i</i>	<i>Track</i>	<i>Date 1</i>	<i>Orbit 1</i>	<i>Date 2</i>	<i>Orbit 2</i>	Δt (days)	B_{\perp} (m)	H_a (m)
Desc.	IS2	23°	435	29-Dec-05	20028	18-May-06	22032	140	41	229
Desc.	IS2	23°	435	09-Mar-06	21030	18-May-06	22032	70	37	254
Desc.	IS2	23°	206	17-May-05	16793	02-May-06	21803	350	52	181
Asc.	IS6	41°	328	25-May-05	16915	14-Jun-06	22426	385	86	109

Table 2. Envisat ASAR data used to produce our interferograms. *Mode* is the Envisat acquisition mode, and *i* is the incidence angle at the centre of the image, measured from the vertical. The first image of each pair was acquired on Date 1, and the second on Date 2, separated by Δt days. The perpendicular baseline between the orbits in each pass is B_{\perp} m., and the altitude of ambiguity H_a m. Interferograms were constructed using GAMMA processing software, and the topographic phase contribution removed using SRTM topography.

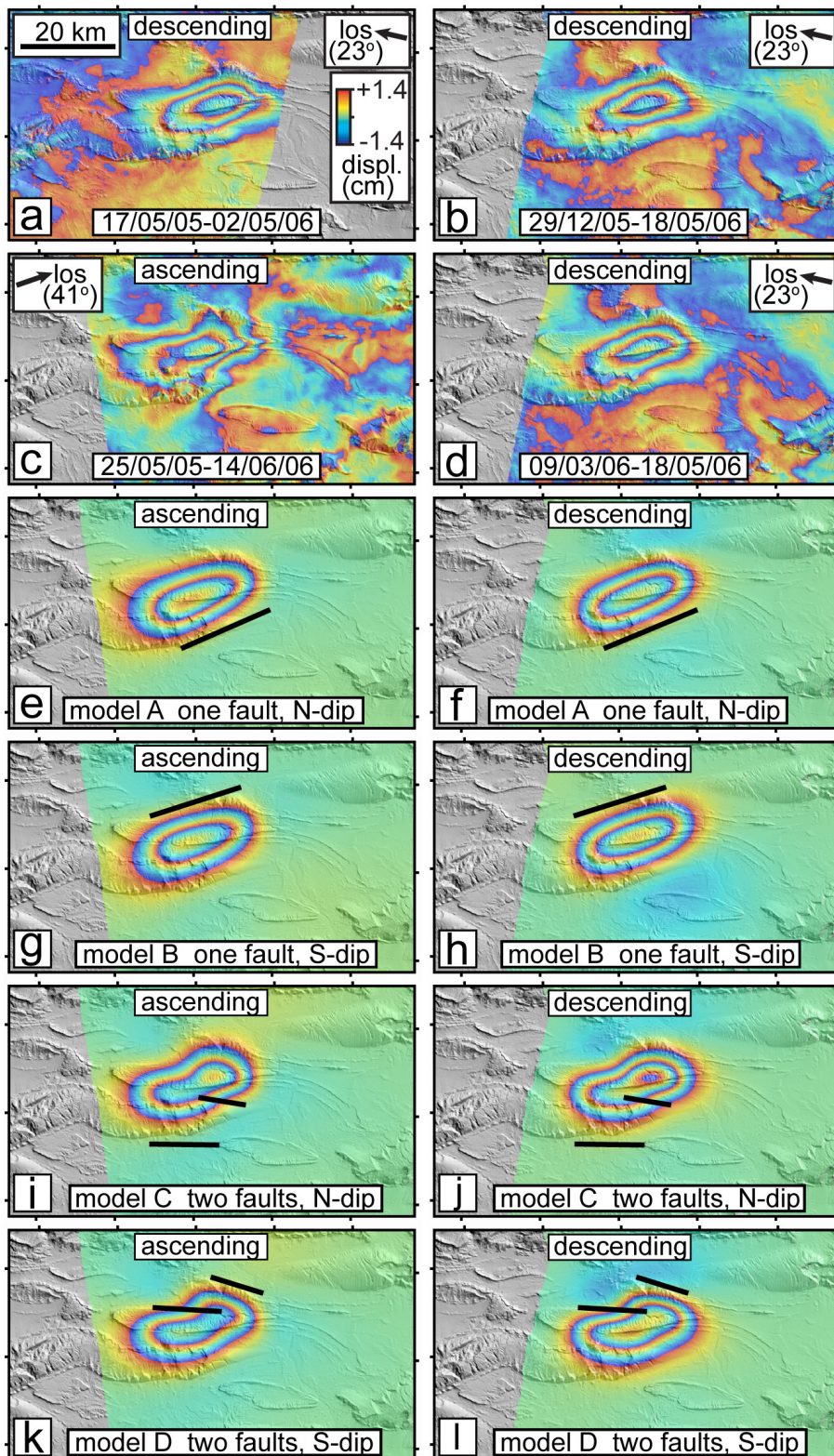


Figure 6. Observed (a–d) and model (e–l) interferograms spanning the 2006 Fin earthquakes, overlain on sun-shaded SRTM topography and with the same map extents as Fig. 2. Each cycle of colour (or fringe) represents a displacement of one radar wavelength (~ 2.8 cm) in the satellite line-of-sight. Black lines show the surface projection of the model fault planes.

<i>Date</i>	<i>Time</i>	<i>Latitude</i>	<i>Longitude</i>	<i>Depth (km)</i>	<i>No.</i>	<i>Gap</i>	<i>Dmin</i>	<i>RMS</i>	<i>Ez (km)</i>	<i>Eh (km)</i>	<i>Ex</i>	<i>S-P</i>	<i>P</i>
12 Apr	17:34	27° 33.98'	55° 49.16'	14.5	15	176	18.1	0.23	4.9	7.3	2.5	3	2
12 Apr	22:42	27° 34.75'	55° 52.66'	17.0	10	163	14.9	0.10	3.6	5.3	1.7	3	2
13 Apr	00:46	27° 34.45'	55° 49.65'	15.3	18	172	17.0	0.30	4.7	6.8	2.5	3	2
13 Apr	01:04	27° 36.93'	55° 49.73'	16.2	8	158	12.9	0.32	13.1	17.5	5.0	3	2
13 Apr	01:14	27° 36.22'	55° 48.86'	15.3	6	184	14.8	0.05	4.4	7.0	1.6	3	2
13 Apr	01:28	27° 34.71'	55° 49.71'	15.0	26	170	16.5	0.43	5.1	7.0	2.7	3	2
13 Apr	02:17	27° 33.35'	55° 49.02'	10.1	16	180	19.3	0.46	8.8	16.7	4.0	3	2
13 Apr	02:29	27° 34.12'	55° 49.92'	16.1	9	173	17.3	0.17	6.0	9.5	2.7	2	2
13 Apr	02:43	27° 38.02'	55° 50.23'	15.6	11	151	10.8	0.33	10.9	13.7	4.2	3	2
13 Apr	02:56	27° 32.67'	55° 52.52'	13.6	22	175	18.8	0.49	5.9	8.6	3.2	3	2
13 Apr	05:53	27° 33.34'	55° 52.08'	14.1	12	172	17.7	0.17	4.0	7.9	2.1	3	2
14 Apr	17:06	27° 40.73'	55° 46.86'	16.1	7	163	12.5	0.05	3.3	4.4	1.4	4	3
14 Apr	20:41	27° 37.04'	55° 42.67'	19.5	9	174	16.6	0.07	3.5	3.7	1.5	4	3
15 Apr	15:45	27° 32.13'	55° 52.98'	8.8	8	176	6.1	0.17	4.2	5.1	2.6	3	3
16 Apr	18:28	27° 38.13'	55° 47.20'	16.1	14	156	14.2	0.13	3.0	3.4	1.4	4	3
17 Apr	02:20	27° 37.42'	55° 44.06'	19.7	8	181	19.2	0.16	6.0	6.6	2.5	4	3
18 Apr	00:51	27° 35.75'	55° 44.85'	18.8	13	177	18.5	0.14	3.8	4.1	1.7	4	3
19 Apr	03:36	27° 34.81'	55° 42.25'	15.2	14	137	18.0	0.23	4.4	7.8	1.7	5	4
19 Apr	19:20	27° 33.69'	55° 46.20'	15.4	21	142	16.0	0.27	3.9	5.6	1.6	5	4
19 Apr	22:11	27° 38.55'	55° 34.77'	19.0	10	122	4.4	0.31	9.9	9.3	5.3	3	3
20 Apr	04:41	27° 37.74'	55° 47.03'	19.2	8	159	16.1	0.14	7.0	8.1	2.9	2	4
20 Apr	06:26	27° 34.82'	55° 45.48'	16.3	26	137	17.2	0.64	6.9	8.9	3.0	5	4
20 Apr	10:06	27° 35.48'	55° 38.41'	21.3	17	131	12.5	0.35	6.1	7.9	3.1	4	4
20 Apr	15:09	27° 37.12'	55° 34.11'	14.9	6	130	6.5	0.06	3.9	4.8	2.1	3	4
20 Apr	18:20	27° 35.66'	55° 43.58'	18.0	15	133	21.7	0.20	3.9	5.0	1.5	5	4
21 Apr	08:40	27° 37.37'	55° 31.42'	21.9	20	171	6.8	0.37	6.8	5.7	3.9	5	4
22 Apr	03:22	27° 32.18'	55° 32.22'	11.7	19	144	13.8	0.25	5.1	8.5	3.8	4	4
22 Apr	05:28	27° 33.35'	55° 29.94'	13.0	5	152	11.6	0.04	5.9	7.1	5.0	2	4
22 Apr	22:57	27° 32.96'	55° 31.10'	15.9	12	136	12.7	0.37	8.1	11.1	5.6	5	4
23 Apr	02:10	27° 36.88'	55° 34.67'	17.9	10	118	7.2	0.18	4.9	6.1	2.7	4	4
25 Apr	01:27	27° 32.00'	55° 38.89'	16.6	10	152	18.3	0.27	7.1	15.0	3.6	4	4
26 Apr	05:02	27° 35.32'	55° 39.25'	15.6	14	133	13.7	0.37	7.5	11.5	3.1	4	4
28 Apr	00:54	27° 36.16'	55° 47.19'	18.8	9	168	14.9	0.18	4.9	5.3	2.3	4	3
28 Apr	01:24	27° 35.32'	55° 47.56'	18.0	22	172	14.0	0.34	4.9	4.6	2.6	4	3

<i>Date</i>	<i>Time</i>	<i>Latitude</i>	<i>Longitude</i>	<i>Depth (km)</i>	<i>No.</i>	<i>Gap</i>	<i>Dmin</i>	<i>RMS</i>	<i>Ez (km)</i>	<i>Eh (km)</i>	<i>Ex</i>	<i>S-P</i>	<i>P</i>
28 Apr	15:23	27° 35.57'	55° 47.01'	16.7	10	172	14.9	0.13	4.2	4.8	2.0	4	3
28 Apr	16:02	27° 35.87'	55° 47.33'	16.5	9	170	14.5	0.04	2.6	3.1	1.3	4	3
29 Apr	02:05	27° 36.03'	55° 45.32'	15.4	15	131	19.0	0.45	7.5	10.8	2.9	5	4
30 Apr	17:49	27° 35.54'	55° 47.21'	21.9	13	172	17.5	0.23	4.5	5.1	2.3	3	2
06 May	04:16	27° 32.94'	55° 29.04'	13.0	25	157	9.9	0.46	5.7	7.0	4.5	4	3
06 May	06:39	27° 33.14'	55° 28.95'	12.9	11	160	10.1	0.16	5.0	6.2	4.0	4	3
06 May	22:36	27° 34.01'	55° 27.86'	12.4	10	183	10.1	0.24	6.3	7.2	5.2	4	3
07 May	23:53	27° 31.71'	55° 42.43'	18.0	14	170	22.1	0.28	4.9	8.5	2.0	4	3
08 May	09:49	27° 33.50'	55° 28.46'	13.5	7	170	10.0	0.20	9.1	11.7	7.3	3	3
10 May	13:51	27° 31.05'	55° 41.71'	23.8	10	158	22.3	0.21	9.3	18.2	4.4	3	3
11 May	01:28	27° 35.61'	55° 35.83'	15.1	8	143	10.0	0.20	7.4	10.7	4.2	4	3
12 May	08:40	27° 34.34'	55° 47.61'	13.4	13	138	18.8	0.36	6.5	14.1	2.4	4	3
12 May	08:47	27° 34.06'	55° 47.73'	4.5	13	140	19.2	0.47	6.7	36.4	3.0	2	2
12 May	16:05	27° 34.67'	55° 46.44'	17.1	18	174	30.0	0.43	7.4	12.5	2.4	2	2
12 May	21:09	27° 34.86'	55° 46.44'	21.1	12	136	19.3	0.22	5.3	8.7	1.9	4	3

Table 3. 49 selected, locally-recorded aftershocks. *No.* is the number of stations that recorded the event; *Gap* is the largest azimuthal gap between these stations; *S-P* is the number of S and P arrivals recorded at the closest five stations, and *P* is the number of P arrivals at the closest four.

<i>Layer</i>	<i>V_p</i>	<i>Depth of top</i>
1	5.7 km/s	0 km
2	6.0 km/s	6 km
half-space	6.75 km/s	16 km

Table 4. Our preferred velocity structure, determined by inverting the arrival-times of the 49 best-recorded aftershocks (for the period 12 April 2006 to 29 May 2006), using the approach of Tatar et al. (2005).